A&A 437, 159–168 (2005)
DOI: 10.1051/0004-6361:20041883

Astronomy & Astrophysics

A cold globule with a Class 0/I embedded source⋆

ISO observations of the dark cloud DC 303.8–14.2

K. Lehtinen[1], K. Mattila[1], and D. Lemke[2]

[1] Observatory, Tähtitorninmäki, PO Box 14, 00014 University of Helsinki, Finland
e-mail: kimmo.lehtinen@helsinki.fi
[2] Max-Planck-Institut für Astronomie, Königstuhl 17, 69117 Heidelberg, Germany

Received 23 August 2004 / Accepted 25 February 2005

Abstract. Infrared observations of the dark cloud DC 303.8–14.2 and the embedded point source IRAS 13036–7644 have been made with the ISOPHOT instrument aboard ISO at 7.7 μm, 60 μm, 100 μm and 200 μm. We have compared the properties of dust in DC 303.8–14.2 and the Thumbprint Nebula (TPN), a morphologically similar globule but without star formation. The dust temperature at the center of DC 303.8–14.2 has a minimum of 14.6 ± 1 K, similar to that in the TPN. A comparison of far-infrared radial optical depth distributions between these clouds at angular scales of ∼1.5′–3′ shows no difference. The observations suggest that there is a bright rim of 7.7 μm emission that peaks just outside the optical bright rim of the cloud, indicating a halo of very small dust particles or PAHs around the cloud. The bolometric luminosity of the IRAS source is estimated to be about 1.0 $L_\odot$. The heating of the cloud by the IRAS source is negligible; the thermal structure of the cloud is dominated by external heating. We have studied the evolutionary status of the IRAS source and find it to be located between Class 0 and Class I, at a late accretion phase. The source was detected at 7.7 μm and we suggest that this emission is due to the 7.7 μm *UIR* band. We also give a compilation of small molecular clouds whose extended FIR emission has been mapped with ISO.

Key words. stars: formation – ISM: clouds – ISM: individual objects: DC 303.8–14.2 – Infrared: ISM – ISM: individual objects: IRAS 13036–7644

1. Introduction

The dark cloud DC 303.8–14.2 (Hartley et al. 1986; Bourke et al. 1995) is a roundish globule-type cloud with an optical diameter of about 10′. It is located in the eastern part of the Chamaeleon II dark cloud complex, at a distance of about 150 pc (Knude & Høg 1998). The dust particles in the cloud scatter the photons of the general interstellar radiation field producing a bright rim-dark core structure at optical wavelengths (see Fig. 1). The point source IRAS 13036–7644 (α(2000) = $13^h7^m36.0^s$, δ(2000) = −77°0′4″) is located near the north-eastern edge of the cloud. Its flux densities in 12 μm, 25 μm, 60 μm and 100 μm IRAS bands are 0.10, 1.08, 6.28 and 22.01 Jy, respectively (Prusti et al. 1992). The SED rises between 12–100 μm, and thus the IRAS source has been classified as a Class I young stellar object (YSO) (Gauvin & Strom 1992). Henning et al. (1993) have measured a 1.3 mm continuum flux density of 223 ± 49 mJy for the IRAS source. The emission is most probably thermal emission from cold circumstellar dust.

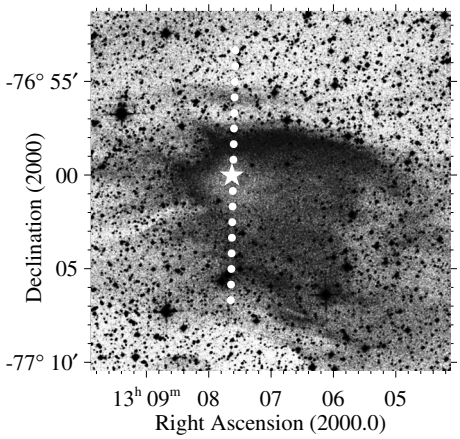

Fig. 1. Digital Sky Survey red band image of DC 303.8–14.2. The brightness scale is inverted. The 7.7 μm and 60 μm strip scan positions are indicated with dots and the position of IRAS 13036–7644 is marked with an asterisk.

The kinematical state of the gas in the cloud, derived from molecular line observations, is ambiguous. Lehtinen (1997) has

⋆ Based on observations with ISO, an ESA project with instruments funded by ESA Member States (especially the PI countries: France, Germany, the Netherlands and the UK) and with the participation of ISAS and NASA.

found that towards the IRAS source the high density tracers CS(J = 2−1), CS(J = 3−2) and $H_2CO(2_{12}-1_{11})$ show asymmetrical double-peaked profiles with a brighter blue-shifted component; such profiles are characteristic of a collapsing cloud. On the other hand, HCO^+(1–0) and ^{12}CO(1–0) lines show a reversed line profile asymmetry, indicating outward motions.

IRAS 13036–7644 is located at the center of a bipolar molecular outflow, thus it is probably the driving source of this outflow (Lehtinen 1997).

IRAS 13036–7644 was studied in the J, H and K bands by Santos et al. (1998). There was neither a red stellar object nor extended nebulosity detected. They concluded that the IRAS source is a very young, deeply embedded source.

Garay et al. (2002) observed silicon monoxide SiO and methanol CH_3OH emission from DC 303.8–14.2. Methanol was detected as a narrow line at the ambient cloud velocity, while no silicon monoxide was detected. This behaviour, together with the fact that in DC 303.8–14.2 the methanol abundance is relatively less enhanced than in more genuine Class 0 objects, led them to conclude that the IRAS source is at a later evolutionary stage at which the strength of the outflow has declined.

For deeply embedded objects like IRAS 13036–7644 the dust envelope reprocesses the luminous energy from the star to IR-radiation and therefore it is necessary to measure the SED in the FIR where the bulk of the emission is located. In the absence of flux measurements between 100 μm and 1.3 mm it has neither been possible to deduce reliably the YSO class of the IRAS source nor to derive the dust temperature and mass. Our ISO data are essential because the maximum of the SED is expected at about 200 μm. The shape of the SED can be used to classify the YSOs into different evolutionary classes.

Theories of isolated, low-mass star formation predict a radial density distribution of matter before and during the star formation process. The density distribution is a critical parameter for these theories because the mass infall rate during the protostellar phase depends on the core density profile at the beginning of the collapse phase. The Thumbprint Nebula (hereafter TPN) is a globule morphologically similar to DC 303.8–14.2, but the TPN has no signs of star formation (Lehtinen et al. 1998). Both globules are located close to each other in the Chamaeleon II/III region. These clouds provide an excellent pair to study the differense between a star forming and a non-star forming globule.

Due to their regular morphologies and sharp edges, DC 303.8–14.2 and TPN are well suited to study the potential existence of a halo-like distribution of very small grains or PAH particles, as suggested by observations and models (Bernard et al. 1992; Bernard et al. 1993). For this purpose we have made strip scans through DC 303.8–14.2 and TPN with a filter encompassing the strong *UIR* band at 7.7 μm.

2. Observations and data reduction

The observations were performed with the ISOPHOT (Lemke et al. 1996) instrument aboard the ISO (Kessler et al. 1996) satellite. We used the observing mode PHT 22, i.e. a raster map on a two-dimensional regular grid. The TDT numbers of the 7.7 μm, 60 μm, 100 μm and 200 μm observations of DC 303.8−14.2 are 71901321, 71901422, 71901220 and 71901119, respectively. The observations of DC 303.8–14.2 were made on November 6th 1997.

Table 1. The properties of filters and sizes of maps made with each filter. $\lambda_{\rm ref}$ is the reference wavelength, $\Delta\lambda$ is the width. $d_{\rm Airy}$ is the diameter of the Airy disk.

Filter	$\lambda_{\rm ref}$ [μm]	$\Delta\lambda$ [μm]	$d_{\rm Airy}$ [″]	Pixel/aperture size [″]	Map size [′]
P1_7.7	7.7	0.84	6.4	52	14×0.8
C_60	60	23.9	50.3	43.5×43.5	13×2
C_100	100	43.6	83.9	43.5×43.5	23×22
C_200	200	67.3	168	89.4×89.4	21×21

The C100 camera (our 60 and 100 μm observations) is a 3×3 pixel array, and the distance between the pixel centers is 46.0″. For the C200 camera (2×2 pixel array) the distance is 92.0″. The relatively narrow 7.7 μm filter is centered on the 7.7 μm Unidentified Infrared feature. For details see Table 1.

The mapped area is about $22' \times 22'$ at 100 μm and 200 μm. At 7.7 μm and 60 μm we performed a strip scan with a length of about 13′ across the IRAS source. In the 100 μm map the distances of raster points in the in-scan and cross-scan directions are 135″ (i.e. full detector width) and 90″ (one pixel overlap). In the 200 μm map both grid steps are 180″ (full detector width). The 100 μm and 200 μm maps have a rotation angle (from north to east) of 25°. At 7.7 μm and 60 μm the linear scans have a rotation angle of 179°, and the distance between raster positions is 50″. The pixel sizes used in the final maps at 60 μm, 100 μm and 200 μm are 45″, 45″ and 90″, respectively.

The data analysis is based on the PIA[1] (ISOPHOT Interactive Analysis) V 8.1. (Gabriel et al. 1997). The detector ramps were corrected for non-linearity, and glitches in ramps were removed by using the two threshold glitch recognition method. The ramps were fitted with 1st order polynomials. Orbital-position dependent dark currents were subtracted. For the flat-field correction we have applied a statistical method: we correlate the value of the reference pixel, at each raster position, against other pixels. Rather than comparing the reference pixel only with pixels belonging to the same raster position, we take a mean of two particular pixels located symmetrically around the reference pixel. This reduces the scatter in the pixel-to-pixel relation caused by a surface brightness gradient in the image.

For the intensity calibration, each raster map is bracketed with faint calibration source (FCS) measurements of 32 s, which determine the actual responsivity of the pixels at the time of the observation. The C100 camera has signal transients during the FCS measurement. Asymptotic

[1] The ISOPHOT data presented in this paper were reduced using PIA, which is a joint development by the ESA Astrophysics Division and the ISOPHOT Consortium (the ISOPHOT Consortium is led by the Max-Planck-Institute for Astronomy (MPIA), Heidelberg). Contributing ISOPHOT Consortium institutes are DIAS, RAL, AIP, MPIK, and MPIA.

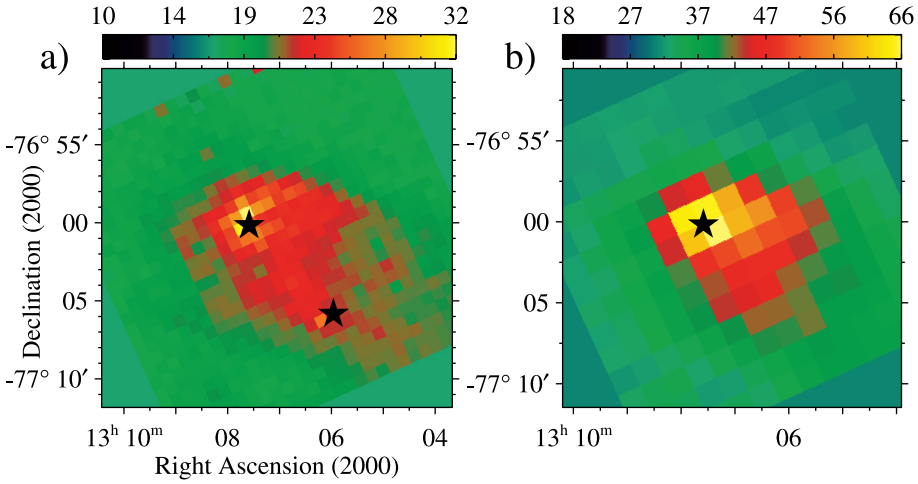

Fig. 2. Maps of the surface brightness at 100 μm **a**), and 200 μm **b**), excluding the emission from the point sources. Intensity scale is given in M Jy sr^{-1}. Estimated zodiacal light values of 1.5 and 0.2 MJy sr^{-1} at 100 μm and 200 μm, respectively, have been subtracted. The positions of the IRAS sources IRAS 13036–7644 (*left*) and IRAS 13022–7650 (*right*) are marked with asterisks. A colour version of the figure is provided in the electronic version of the paper.

values of the signal were derived by applying the drift modelling of PIA. The surface brightnesses derived this way are in excellent agreement with the COBE/DIRBE[2] (`http://lambda.gsfc.nasa.gov/product/cobe`) data (for details of the comparison see Lehtinen et al. 1998; Lehtinen et al. 2000; Lehtinen et al. 2001). The C200 camera signal is stable during the FCS measurements and thus no drift modelling is required. The absolute accuracy of the ISO data is estimated to be 25% at all wavelengths.

Based on the zodiacal emission model of Good (1994), the value of the zodiacal light at the time and position of observations at 7.7 μm, 60 μm, 100 μm and 200 μm is estimated to be 5.7, 5.7, 1.5 and 0.2 MJy sr^{-1}, respectively.

3. Observed properties of DC 303.8–14.2

3.1. General characteristics

An optical red band Digital Sky Survey image ("Second Epoch Southern survey" UK Schmidt IIIaF + RG610) is shown in Fig. 1. The globule is characterized by a bright rim due to scattered light of the Interstellar Radiation Field (ISRF). At the bright rim the optical depth through the cloud is $1.5^{\rm m}$–$2^{\rm m}$ which is optimum for scattering. At optical wavelengths the shape of the cloud is cometary, with a sharp edge at the north-eastern side, and a tail pointing to the south-west. The IRAS source is located at the head of the cloud, near the steep density gradient. Images of the surface brightness at 100 μm and 200 μm are shown in Fig. 2.

In addition to IRAS 13036–7644, we have detected at 100 μm the source IRAS 13022–7650, which is the variable star DL Cha (Kukarkin et al. 1971). This source is listed as a field star by Hughes & Hartigan (1992). The IRAS point source catalog gives an upper limit of 2.4 Jy at 100 μm for this source, while we derive a flux of about 0.6 Jy.

3.2. Temperature distribution

In order to derive the dust temperature for the extended emission of the cloud, we first have to subtract the emission of the IRAS source. By comparing the point-source template of ISOPHOT (footprint matrix) with the brightness profile of the IRAS source we find the profile to be well characterized by a point source profile, both at 100 μm and 200 μm. In the 100 μm map the extended emission can be well separated from the emission of the IRAS source, thus the observed emission at the core of the cloud has been fitted with a combination of a Gaussian surface and a point source profile (see Fig. 3 a, b). In the 200 μm map, with a lower resolution, it is more difficult to separate the contributions from the cloud and the point source. On the other hand, our near-IR extinction data (Lehtinen et al., in preparation) show that the maximum extinction is located at the position of the IRAS source. Furthermore, the $C^{18}O$ column density map (Kainulainen 2004) shows that the IRAS source is located close to the column density maximum of molecular material. As can be seen in Figs. 3c and d, the extended emission is not symmetric with respect to the IRAS source. Thus we cannot fit the extended emission with a single Gaussian surface having its maximum at the position of the IRAS source.

The position of the IRAS source, derived from the 100 μm map, is close to the center of a group of four pixels in the 200 μm map. Based on the footprint matrix we then know that most of the emission from the point source is within these four pixels. Thus, we have fitted only two rows of the 200 μm image, those rows that underlie the IRAS source. Both rows are fitted with two Gaussians, one for the pixels on the leftward side of the IRAS source and another for the pixels on the rightward side. These two Gaussians are forced to have their maximum at the position of the IRAS source, and to have equal peak intensities. The fitted point source profiles were then

[2] The COBE datasets were developed by NASA funding and resources through the NASA Goddard Space Flight Center under the guidance of the COBE Science Working Group and were provided by the NSSDC.

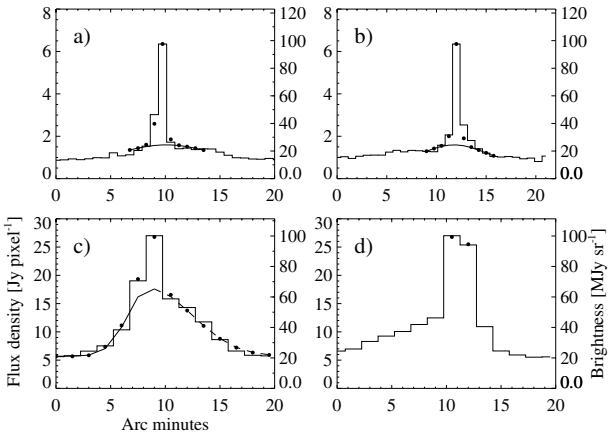

Fig. 3. Scans through the cloud along rows and columns of the images at 100 μm, **a), b)** and 200 μm, **c), d)**. The scans go through the image pixel located closest to the fitted position of IRAS 13036–7644. Panels **a)** and **c)** are along the rows (approximately from East to West), **b)** and **d)** along the columns (approximately from South to North). Zodiacal light has not been subtracted. The histogram is the observed distribution, the solid or dashed line is the Gaussian fit to the extended emission excluding the IRAS source. The dots show the total fitted emission. In panel **c)** we have fitted the leftward side (solid line) and the rightward side (dashed line) of the cloud separately (see Sect. 3.2 for details). In panel **d)** we show only the total fitted emission at the position of the IRAS source.

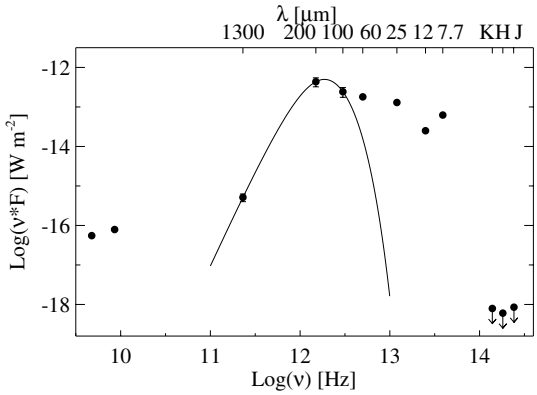

Fig. 4. The spectral energy distribution of IRAS 13036–7644. The data points are, from shortest to longest wavelength, VLT/ISAAC near-IR $J/H/K_s$ data, ISOPHOT 7.7 μm data, IRAS 12 μm and 25 μm data, ISOPHOT 60 μm, 100 μm and 200 μm data, SEST 1.3 mm bolometer (Henning et al. 1993) data and radio continuum 3 cm and 6 cm (Lehtinen & Higdon 2003a) data. The solid line is a modified blackbody fit to the 100 μm, 200 μm and 1300 μm data points and results in a temperature of 20.0 K.

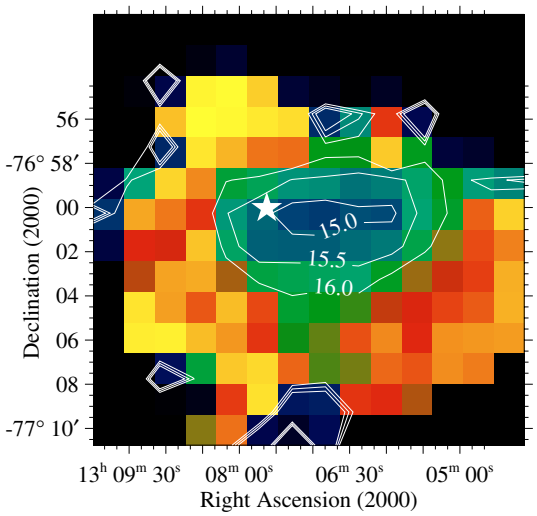

Fig. 5. Map of the dust temperature derived from 100 μm and 200 μm data. The temperature is derived for extended emission only. The position of IRAS 13036–7644 is marked with an asterisk. Due to the background subtraction the temperature outside the cloud cannot be determined. The contours are at 15.0 K, 15.5 K and 16.0 K. A colour version of the figure is provided in the electronic version of the paper.

subtracted from the observed intensity maps to obtain maps of extended emission without the IRAS source. In Fig. 3 we show scans through the IRAS source along rows and columns of the ISOPHOT maps at 100 μm and 200 μm. The histogram is the observed distribution, the solid or dashed line is a Gaussian fit to the extended emission and the dots show the total fitted emission.

We then subtracted a constant value representing the background emission around the cloud (13.4 MJy sr^{-1} at 100 μm, 19.6 MJy sr^{-1} at 200 μm), and finally convolved the 100 μm image to the resolution of the 200 μm image. The surface brightness of the extended emission at the cloud center is about 14 MJy sr^{-1} and 46 MJy sr^{-1} over the background, at 100 μm and 200 μm, respectively. The 100 μm and 200 μm images have then been fitted with a modified blackbody of the form $I(\lambda) \propto \lambda^{-\alpha}\, B(\lambda, T_{\rm dust})$, with $\alpha = 2$. An image of the derived dust temperature for the extended emission is shown in Fig. 5. The minimum dust temperature is about 14.6 K. The IRAS source is located close to the temperature minimum.

The presence of a weak molecular outflow (Lehtinen 1997) and possible Herbig-Haro objects (Lehtinen et al. 2003) in DC 303 raises the question of whether dust is heated through interaction with the outflow, either through collisional or ultraviolet heating. However, observations have shown that the impact of outflows on dust, if detected at all, is very local. Dent et al. (2003) have argued that a sub-mm continuum peak with a *FWHM* size of about 20″ is heated by local shocks from the outflow jet in the Herbig-Haro object HH2. Chini et al. (2001) have found enhanced mm/sub-mm dust emission from CO outflows or Herbig-Haro objects around HH 7–11, L 1157 and IRAS 23011+6126, with sizes less than one arcminute. On the other hand, Morris et al. (2004) did not find indication of warm dust in the strong outflow of NGC 7129 at wavelengths of 10−35 μm. We may then conclude that the effects of the weak outflow on dust in DC 303 are negligible with our resolution of ∼90″.

Note that the temperature, as well as the optical depth, derived in the next section are average values over the beam area at 200 μm.

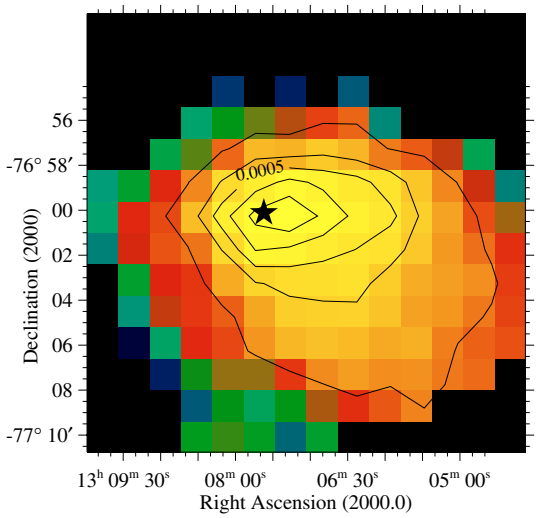

Fig. 6. Map of 200 μm optical depth, excluding the contribution from the IRAS sources. The contours are 1, 3, 5, 7 and 9×10^{-4}. The position of IRAS 13036–7644 is marked with an asterisk. A colour version of the figure is provided in the electronic version of the paper.

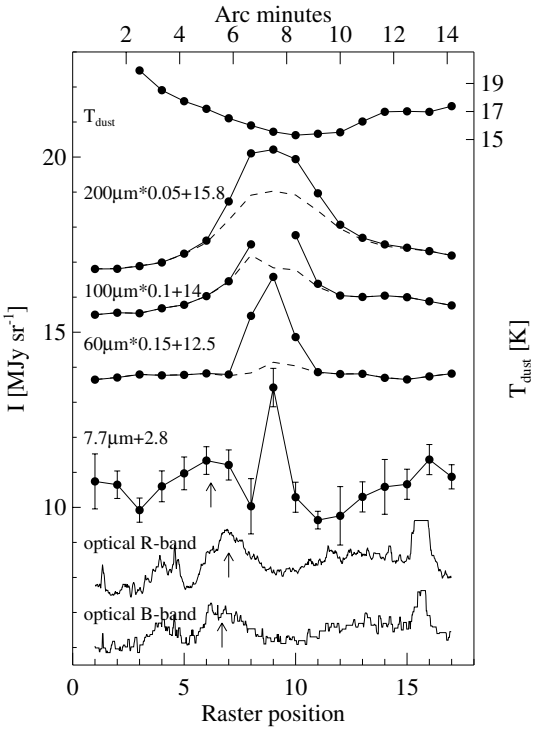

Fig. 7. Intensity profiles through DC 303.8–14.2 along the raster positions of the 7.7 μm data, from North (position 1 on left) to South (see Fig. 1). IRAS 13036–7644 is located at position number 9. The brightness scale is valid for ISO data only. The scale of the optical red and blue band data is arbitrary. The right-hand y-axis is valid for dust temperature. Solid lines show the total intensity. For the case of 100 μm intensity the brightest emission at the IRAS position has been excluded from the plot. Dashed lines show the intensity after subtracting the fitted point-source template of the IRAS source. Zodiacal emission has not been subtracted from the ISO data. The arrows show the positions of the optical and 7.7 μm surface brightness maxima at the Northern edge of the cloud (see Fig. 1).

3.3. Optical depth and mass of dust

For optically thin emission the optical depth τ_ν is related to the observed intensity I_ν and blackbody emission $B_\nu(T_\mathrm{d})$ via

$$\tau_\nu \approx I_\nu / B_\nu(T_\mathrm{d}). \quad (1)$$

The derived optical depth map at 200 μm, with a maximum of $\tau \approx 1.2 \times 10^{-3}$, is shown in Fig. 6.

The total mass (gas plus dust) of the cloud has been calculated from

$$M = \frac{F_{200\ \mu\mathrm{m}} D^2 m_\mathrm{H} \mu}{B(200\,\mu\mathrm{m}, T_\mathrm{d}) \sigma_\mathrm{H}(200\,\mu\mathrm{m})} \quad (2)$$

where $F_{200\ \mu\mathrm{m}}$ is the observed flux density, D the distance, m_H the mass of one hydrogen atom, μ the mean molecular weight, $B(200\ \mu\mathrm{m},T_\mathrm{d})$ the blackbody emission at temperature T_d and σ_H the absorption cross section per H-nucleus for which we have used the value 2.5×10^{-25} cm^2 (Lehtinen et al. 1998). The mass was calculated pixel by pixel. The mass inside the $\tau_{200\ \mu\mathrm{m}} = 3 \times 10^{-4}$ contour in Fig. 6 is ~2.7 $M_\odot$, with an uncertainty by a factor of two.

3.4. Bright rim at 7.7 μm

The 7.7 μm surface brightness along the raster scan is shown in Fig. 7. Also plotted are cuts through the cloud in the optical blue and red bands, at far-IR wavelengths, and through the temperature map. IRAS 13036–7644 is detected at 7.7 μm at raster position number 9. The optical surface brightness peaks at the bright rim of the cloud, at raster positions ~6–8 and ~13–16, as can also be seen in Fig. 1. The underlying 7.7 μm surface brightness distribution follows this same trend, i.e. it has a bright rim-dark core structure (excluding the IRAS source). It is notable that the 7.7 μm maximum brightness is located at the outer edge of the maximum optical surface brightness. Outside the cloud, 7.7 μm emission is dominated by zodiacal light; the observed intensity of about 8 MJy sr^{-1} is in good agreement with the model-based zodiacal light intensity of about 6 MJy sr^{-1} (see Chap. 2).

Bernard et al. (1992) have shown that the limb brightening observed in several clouds at 12 μm and 25 μm IRAS bands cannot be explained solely by radiative transfer effects, but enhancement in the abundance of the smallest dust particles is required. The suspected PAH particles form a halo around the cloud. According to Bernard et al. (1993) the halo is located at the cloud edge where visual extinction is between $0^\mathrm{m} < A_\mathrm{V} < 0.5^\mathrm{m}$. This is in a good agreement with the 7.7 μm surface brightness profile of DC 303 (see Fig. 7); the maximum brightness at raster position #6 occurs outside the optical surface brightness maximum where the visual extinction through the cloud is ~1.5^m–2^m. This also indicates that the very small dust particles or PAHs responsible for the 7.7 μm emission would be mainly excited by UV-photons, not by optical photons.

An alternative explanation for the 7.7 μm surface brightness halo is by means of radiative transfer effects, i.e. that UV-optical radiation exciting the particles emitting at 7.7 μm undergoes rapid extinction at the edge of the cloud.

In the case of TPN we have made a similar raster scan measurement through the cloud center (TDT No. 71901524) extending beyond the optical extent of the globule, but the surface brightness of TPN is not detected at 7.7 μm.

4. The embedded source IRAS 13036–7644

The emission from the IRAS source has been fitted with a point source template of the ISOPHOT, as described in Sect. 3.2. The derived point-source fluxes are 4.1 Jy, 8.1 Jy and 29.0 Jy at 60 μm, 100 μm and 200 μm, respectively. The 60 μm and 100 μm fluxes are about half of the IRAS fluxes, which can be explained by the better background separation achieved by ISO.

As shown in Fig. 4, the intensity is expected to decrease at wavelengths shorter than 12 μm, but the observed 7.7 μm flux shows the opposite behaviour. We interpret the observed 7.7 μm emission at the position of the IRAS source as emission from the 7.7 μm *UIR* band, not as continuum emission. However, we cannot rule out the presence of a spatially separate component of hot dust near the IRAS source, leading to increased continuum emission. For the flux at 7.7 μm we take the flux at the IRAS source position in excess of the two adjacent raster positions, giving 0.16 Jy. At 2.2 μm we derive, from VLT/ISAAC imaging, a limit of $\geq$22.7 mag, corresponding to $\leq 5.7 \times 10^{-7}$ Jy (Lehtinen et al., in preparation).

There are few observations of the 7.7 μm UIB feature in young stellar objects. Examples of Herbig Ae/Be type stars are HD 97048 with an intensity of 1.2×10^{-13} W m^{-2} in a 5″ aperture (Schutte et al. 1990), and VLA 4 in the star forming region GGD 14 with an intensity of 6.5×10^{-13} W m^{-2} in a 24″ aperture (Persi & Tapia 2003). To our knowledge, the integrated 7.7 μm flux of IRAS 13036–7644, about 7×10^{-15} W m^{-2} in a 52″ aperture, is the weakest flux observed towards any YSO.

4.1. The spectral energy distribution

The spectral energy distribution of IRAS 13036–7644 is shown in Fig. 4. The emission at 100 μm, 200 μm and 1300 μm wavelengths is expected to originate from "classical", large cold dust grains which are at an equilibrium temperature determined by the surrounding radiation field. Thus, we have fitted these flux values with a modified blackbody of the form

$$F_\nu = B_\nu(T_{\rm dust})\,(1 - \exp(-\tau_\nu))\,\Omega_{\rm s} \qquad (3)$$

where $B_\nu(T_{\rm dust})$ is the Planck function at the dust temperature $T_{\rm dust}$, τ_ν is the optical depth which is assumed to vary with frequency as $\tau_\nu = (\nu/\nu_0)^\alpha$, and $\Omega_{\rm s}$ is the solid angle of the emitting region. We have tried different values of the opacity power-law index α between 1–2, and found that the value $\alpha = 2$ gives the best fit. The fitted values are $T_{\rm dust} = 20.0 \pm 3.3$ K, $\lambda_0 = 240 \pm 134\,\mu$m (i.e. the wavelength where the optical depth is unity, corresponding to ν_0), and $\Omega_{\rm s} = 12 \pm 94\,\Box''$. The errors have been estimated with a Monte Carlo method, and show that the value of $T_{\rm dust}$ is well determined, and the current data cannot confine the size of the emitting region nor the wavelength λ_0.

Integrating the fitted blackbody curve we obtain the luminosity of the cold dust $L_{\rm cd} \approx 0.4\ L_\odot$, while the bolometric luminosity of the source is estimated to be $L_{\rm bol} \approx 1.0\ L_\odot$. The sub-millimetre luminosity, $L_{\rm sub-mm}$, which is the integrated luminosity longward of 350 μm, is 0.02 $L_\odot$. This gives a ratio $L_{\rm bol}/L_{\rm sub-mm} \approx 43$.

Clearly it is a simplification to use a single-temperature blackbody fit; fluxes at wavelengths shorter than about 100 μm are higher than accounted for by the fit. This indicates that there is an envelope of dust around the IRAS source with dust particles having a range of temperatures. Some of the emission at $\lambda \lesssim 100\,\mu$m may originate from transiently heated small grains.

At 1.3 mm wavelength the emission is optically thin, so we can estimate the circumstellar dust mass by using the flux at 1.3 mm and the derived dust temperature. Using the formula for the circumstellar mass (e.g. Chini et al. 1987),

$$M_{\rm cs} = \frac{S_\nu D^2}{R \kappa_\nu B_\nu(T_{\rm dust})} \qquad (4)$$

where D is the distance, R is the dust-to-gas mass ratio (assumed to be 1:100) and κ_ν is the mass absorption coefficient of the dust (we use $\kappa_\nu = 1\,{\rm cm^2\,g^{-1}}$ which is applicable in dense clouds and protostellar envelopes, Ossenkopf & Henning 1994), we obtain $M_{\rm cs} \approx 0.1\ M_\odot$. This mass is similar to the observed circumstellar masses of Class I sources, which are typically substellar, <0.1–0.3 $M_\odot$ (Whitney & Hartmann 1993; Kenyon et al. 1993; André & Montmerle 1994; Lucas & Roche 1989). The derived parameters are listed in Table 2, together with parameters for Class 0/I sources as given by Visser et al. (2002), based on IRAS data and sub-mm observations of protostars in Lynds dark clouds.

4.2. The evolutionary status

The three-category classification scheme of YSOs (see e.g. Lada & Wilking 1984; Adams et al. 1987; Lada 1987; Wilking et al. 1989) is commonly used to specify their evolutionary status. Class I objects are the youngest in this scheme, and they are considered to be deeply embedded YSOs with disks and massive circumstellar gas and dust envelopes. In the extended classification scheme the Class 0 sources represent even younger objects, which are in the main accretion phase and which have an envelope mass greater than central stellar mass (André et al. 1993).

A Class 0 object has to satisfy the following criteria (André et al. 1993): (1) non-detectability at wavelengths shorter than about 10 μm; (2) indirect evidence for the existence of a central protostellar object (e.g. a molecular outflow or a continuum source at cm wavelengths); (3) the shape of the SED well characterized by a single modified blackbody with a temperature in the range of about 15–30 K; (4) the ratio $L_{\rm bol}/L_{\rm sub-mm} \ll 200$, where $L_{\rm sub-mm}$ is the luminosity for wavelengths greater than 350 μm. The condition #4 implies that the circumstellar mass is greater than the mass of the central protostellar object. Because a Class 0 object is in the main accretion phase, there should also be evidence of infall motion towards the protostar.

IRAS 13036–7644 satisfies criterion #1; the shortest wavelength where the source has been detected in continuum

Table 2. Derived properties of IRAS 13036–7644, compared to the average properties of Class 0 and Class I protostars from Visser et al. (2002). The position of IRAS 13036–7644 has been determined from the 100 μm map. The errors of the fluxes include statistical errors only. The error of $T_{\rm dust}$ is based on the estimated 25% absolute accuracy of fluxes. $M_{\rm cs}$ is the circumstellar mass. $L_{\rm sub-mm}$ is the luminosity integrated longward of 350 μm. The values given for Class 0/I objects are the mean value and the range of values in square brackets.

Source	Position		$F(7.7\,\mu$m)	$F(60\,\mu$m)	$F(100\,\mu$m)	$F(200\,\mu$m)	$T_{\rm dust}$	$L_{\rm bol}$	$M_{\rm cs}$	$L_{\rm bol}/L_{\rm sub-mm}$	$L_{\rm sub-mm}$
	α(2000)	δ(2000)	[Jy]	[Jy]	[Jy]	[Jy]	[K]	[$L_\odot$]	[$M_\odot$]		[$L_\odot$]
IRAS 13036–7644	$13^{\rm h}07^{\rm m}34.7^{\rm s}$	$-77°00'14''$	0.16 ± 0.03	4.1 ± 0.2	8.1 ± 1.1	29.0 ± 3.4	20.0 ± 3.3	1.0	0.1	43	0.02
Class 0 (Visser et al. 2002)							20.5 [19:27]	4.3 [1.1:9.0]	0.42 [0.16:2.15]	32 [26:91]	0.09 [0.03:0.31]
Class I (Visser et al. 2002)							26.2 [24:28]	1.5 [0.6:11.7]	0.13 [0.01:0.32]	79 [59:250]	0.02 [0.003:0.1]

radiation is 12 μm. Criterion #2 is fullfilled because there is both an outflow and a cm-wavelength continuum source detected. The molecular line profiles observed by Lehtinen et al. (1997) indicating collapse further support the idea that the IRAS source was built up by accretion. For the ratio $L_{\rm bol}/L_{\rm sub-mm}$ we derive a value of about 43 and thus criterion #4 is satisfied. Criterion #3 is not satisfied; only the far-IR and mm-emission are well characterized by a single modified blackbody.

A parameter that uses all the information of a SED is the bolometric temperature $T_{\rm bol}$. It is defined as the temperature of a blackbody which has the same mean frequency (that is the ratio of the first and zeroth frequency moments of the spectrum) as the observed SED (Myers & Ladd 1993). The bolometric luminosity vs. bolometric temperature diagram is a generalized form of the HR diagram and can be used to specify the evolutionary status of deeply embedded YSOs. Chen et al. (1997) have calculated bolometric luminosities and temperatures (as defined in Myers & Ladd 1993) for YSOs in nearby molecular clouds. They find the values of 0.47 $L_\odot$ and 63 K for IRAS 13036–7644. We have estimated the bolometric temperature $T_{\rm bol}$ of the IRAS source, as defined by Myers & Ladd (1993). We use the flux values between 12 μm–1300 μm, and obtain the value $T_{\rm bol} \approx 62$ K. We do not correct the fluxes for the foreground interstellar extinction which is expected to be negligible at the near-IR and longer wavelengths towards the Chamaeleon I cloud, and because the effect of interstellar extinction on the derived value of $T_{\rm bol}$ and $L_{\rm bol}$ is less important for a source with a low $T_{\rm bol}$ (Chen et al. 1995). The bolometric luminosity $L_{\rm bol} \approx 1.0\,L_\odot$, derived in Sect. 4.1, is about two times higher than estimated by Chen et al. (1997). We can now more firmly estimate the evolutionary stage of the IRAS source. In the bolometric luminosity-temperature diagram of Chen (1995) the position of IRAS 13036–7644 is located near the division line between Class 0 and Class I sources. This is in accordance with the finding that some properties of the source support a Class 0 stage while some do not.

Thus, we classify IRAS 13036–7644 as a transition object between evolutionary Classes 0 and I. The object is no longer in the main accretion phase but rather is in the late accretion phase.

Pezzuto et al. (2002) have made a two-colour diagram for YSOs based on 60 μm, 100 μm and 170 μm fluxes. Their sample includes 17 Class 0 sources, with median colors [60−100] $\equiv \log(F(100\,\mu\text{m})/F(60\,\mu\text{m})) = 0.53 \pm 0.23$ and [100−170] $= 0.19 \pm 0.18$. For IRAS 13036–7644 we derive the colors [60−100] = 0.34 and [100−170] = 0.54. The color [60−100] is typical of Class I sources, but the color [100−170] is redder and thus the dust temperature is lower than for any of the sources in the two-colour diagram of Pezzuto et al.

5. Comparison with the Thumbprint nebula and other small clouds

TPN is morphologically similar to DC 303.8–14.2 at optical wavelengths. However, TPN is without an embedded infrared source. TPN has been studied at 100 μm and 200 μm by Lehtinen et al. (1998). We have reanalyzed the TPN data

Table 3. Small molecular clouds whose extended FIR emission has been mapped by ISO. The distances are as given by the different authors. The parameters are given only if they are available based on far-IR maps between 100 μm and 200 μm, except the temperatures of WTAK sources which are based on far-IR and mm/sub-mm data. $T_{\rm dust}$ is the dust temperature for extended emission and has been determined with the dust emissivity index $\alpha = 2$. The values of $\tau^{\rm central}_{200\mu{\rm m}}$ and $N^{\rm central}_{\rm H}$ for the sources CB 236 and CB 220 have been derived from the data given in Richards et al. (1999), assuming an average absorption cross section per H-atom $\sigma_{\rm H} = 2.5 \times 10^{-25}$ cm^2. The value of $\tau^{\rm central}_{200\mu{\rm m}}$ for ISOSS J20246+6540 has been derived from N(H) given by Tóth et al. (2002), assuming $\sigma_{\rm H}$ as above.

Cloud	Distance [pc]	Size [']	Size [pc]	Mass [$M_\odot$]	$T_{\rm dust}$ [K]	$\tau^{\rm central}_{200\mu{\rm m}}$ [10^{-3}]	$N^{\rm central}_{\rm H}$ [10^{22}]	YSO ?	Reference	Notes
DC 303.8–14.2	150	14×10	0.6×0.4	2.7	14.6 ± 1	1.2	0.5	Yes	This study	4, 5, 7
Thumbprint Nebula	200	7	0.4	1.9	13.5 ± 1	0.7	0.3	No	Lehtinen et al. (1998)	4, 5, 7
FS 2–137	140	20	0.8		$13.5^{+1.8}_{-1.7}$			No	Laureijs et al. (1996); FS	4, 5, 8
L 183	100	16	0.5	25	$\lesssim 12$	7	3	No	Juvela et al. (2002)	2, 4, 5, 7
CB 236	600	3.0×1.5	0.5×0.3	1.0	$12.5^{+0.8}_{-1.0}$	0.3	0.1	No	Richards et al. (1999); CB	1, 4, 5, 7
CB 220	600	3.0×4.5	0.5×0.8	3.3	$13.6^{+0.5}_{-0.6}$	0.3	0.1	No	Richards et al. (1999); CB	1, 4, 5, 7
ISOSS J20246+6540	400	$\lesssim 2.5$	$\lesssim 0.3$		<14.5	0.2	0.09	No	Tóth et al. (2002)	3, 6, 9
L 1498	140	7×6	0.3×0.2		10 ± 3			No	WTAK	2, 3, 5, 10
L 1517B	140	4×3	0.2×0.1		10 ± 3			No	WTAK	2, 3, 5, 10
L 1544	140	8×4	0.3×0.2		9 ± 3			No	WTAK; WTMA	2, 3, 5, 10
L 1582A	400	7.4×4	0.9×0.5		15 ± 3			No	WTAK	2, 3, 5, 10
L 183	150	7×5	0.3×0.2		10 ± 3			No	WTAK; WTMA	2, 3, 5, 10
L 1696A	140	5×5	0.2×0.2		10 ± 3			No	WTAK; WTMA	2, 3, 5, 10
L 1689A	140	4×4	0.2×0.2		19 ± 3			No	WTAK	2, 3, 5, 10
L 1689B	140	7×4	0.3×0.2		11 ± 3			No	WTAK; WTMA	2, 3, 5, 10
L 63	160	6×6	0.3×0.3		11 ± 3			No	WTAK; WTMA	2, 3, 5, 10
B 68	200	4×4	0.2×0.2		10 ± 3			No	WTAK	2, 3, 5, 10
B 133	400	8×3	0.9×0.4		13 ± 3			No	WTAK; WTMA	2, 3, 5, 10

Notes – (1) Distance unknown, assumed to be 600 pc; (2) pre-protostellar core; (3) *FWHM* size; (4) total extent of the far-IR emission; (5) size from 200 μm map; (6) size from 170 μm map; (7) $T_{\rm dust}$ based on 100 μm and 200 μm data; (8) $T_{\rm dust}$ based on 135 μm and 200 μm data; (9) $T_{\rm dust}$ based on 170 μm and 200 μm data; (10) $T_{\rm dust}$ based on 170 μm, 200 μm and mm/sub-mm data.
References – FS = Feitzinger & Stuve (1984); CB = Clemens & Barvainis (1988); WTAK = Ward-Thompson et al. (2002); WTMA = Ward-Thompson et al. (1999).

with the same version of PIA in order to have a consistent calibration.

5.1. Dust temperature and column density

The values of the maximum surface brightness at the center of DC 303.8−14.2 are about 2.3 and 2.0 times higher than in the center of the TPN at 100 and 200 μm, respectively. The temperature of dust in DC 303.8−14.2 decreases towards the cloud center, as it does in TPN (Lehtinen et al. 1998). In DC 303.8−14.2 the minimum temperature at the cloud center is 14.6 ± 1 K, whereas in TPN it is 13.5 ± 1 K (both for $\alpha = 2$). Thus the embedded IRAS source inside DC 303.8–14.2 is not able to raise the dust temperature to a significantly higher value than that in TPN. The 200 μm optical depth of DC 303.8–14.2 is $\sim 1.2 \times 10^{-3}$ at maximum, about 1.7 times the maximum value of TPN. However, these values of optical depth are mean values over about a 90″ diameter region, the size of the C200 camera pixel. When measuring dust column density at a higher resolution the differences are greater: for TPN the value of central visual extinction is about 8 mag (Lehtinen & Mattila 1996), while for DC 303.8−14.2 the extinction is >30 mag based on deep near-IR *JHK* imaging with ESO/VLT (Lehtinen et al., in preparation).

5.2. Radial dust density distributions

The extended emission at far-IR is optically thin and thus it traces all the dust along the line of sight, as long as the dust temperature is sufficiently high. The observed optical depth as a function of impact parameter from the cloud center can be inverted to give the radial space density, assuming that the volume density follows a single power law function and that the dust is isothermal (see e.g. Yun & Clemens 1991). TPN has no internal heating source and its far-infrared emission is fully consistent with its dust being heated by the general interstellar radiation field (ISRF) only. For such a cloud the temperature is expected to decrease towards the center, as observed (Lehtinen et al. 1998). On the contrary, the IRAS source within DC 303.8−14.2 could act as a heating source for dust in the cloud. For a centrally heated cloud the temperature decreases from the cloud center to the edge. However, our ISO data show that in DC 303.8−14.2 the dust temperature decreases towards the cloud center, and that there is no temperature enhancement towards the IRAS source (see Fig. 5). Thus we assume that the main heating source for DC 303.8−14.2 also is the ISRF. Because the temperature decreases towards the center in both DC 303.8–14.2 and TPN, we can make a comparative study of their radial optical depth distributions on a qualitative level.

In order to derive the radial optical depth profiles we have used the ellipse-fitting method of Yun & Clemens (1991).

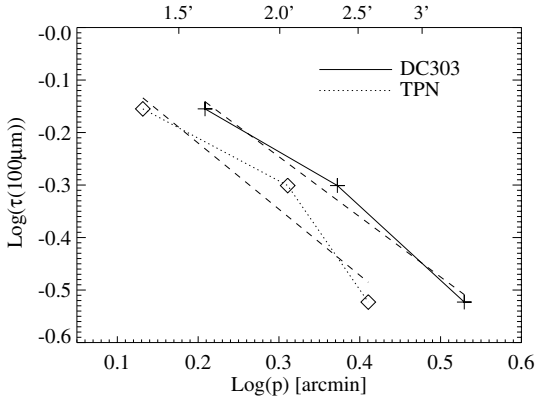

Fig. 8. Radial optical depth profiles of DC 303.8–14.2 and TPN at 100 μm. The dashed lines are linear fits to the data points, giving $\alpha \approx$ 1.2 and 1.3 for DC 303 and TPN, respectively. α is defined as $\log(\tau) = -\alpha \log(p)$. See Sect. 5.2 for details.

One draws contours of equal intensity on the data. We have drawn the contours at 30%, 50% and 70% of the maximum value. In Fig. 8 we show the radial optical depth profiles of DC 303.8−14.2 and TPN at 100 μm (the optical depth at 200 μm is a scaled version of that at 100 μm and would give exactly the same results). Within errors, the radial optical depth profiles can be fitted with straight lines. If an infinite, isothermal cloud has a volume density of dust of the form $\rho(r) \propto r^{-\gamma}$, then the optical depth of dust emission τ as a function of impact parameter p has the form $\tau(p) \propto p^{-\gamma+1} \equiv p^{-\alpha}$. We have derived the values $\alpha \approx 1.2$ and 1.3 for DC 303 and TPN, by using the data points in Fig.8, tracing most of the volume of the clouds. The values of γ are then $\gamma = 1 + 1.2 = 2.2$ and $1 + 1.3 = 2.3$ for most of the volume of DC 303 and TPN, respectively. Within errors, the radial density distributions are similar.

5.3. Comparison with other small clouds

Clemens et al. (1991) derived far-IR fluxes for the small molecular clouds listed in Clemens & Barvainis (1988) by performing aperture photometry at 12 μm, 25 μm, 60 μm and 100 μm on IRAS maps. From the 60 μm and 100 μm flux ratios they derived a mean color temperature of dust of 26 ± 5 K. However, it is now known that part of the 60 μm emission comes from a dust population with smaller grains than the 100 μm emission and thus the temperature derived from the 60 μm to 100 μm intensity ratio does not give accurate results for the so-called "classical large grains".

The properties of "classical" grains, such as temperature and optical depth, can be derived correctly only if we have observations at $\lambda \gtrsim 100$ μm. Table 3 gives the properties of small dark clouds whose extended dust emission has been mapped with ISO at $\lambda \geq 100$ μm. The first three clouds are globule-type clouds located in the Chamaeleon region. L 183 is a dark cloud which has two pre-protostellar cores (Ward-Thompson et al. 1994, 1999; Crutcher et al. 2004). The clouds CB 236 and CB 220 are protostellar candidates (Richards et al. 1999).

The rest of the clouds were originally selected by Ward-Thompson et al. (1994) to be representative of pre-protostellar starless cores. Only the cloud DC 303.8–14.2 shows signs of star formation in the form of an embedded IRAS source. The dust temperatures are concentrated in a narrow range around ∼13.5 K. On the other hand, the dust column densities vary by a factor of about 20. It has been found that the ISRF is intense enough to be the only heating source of dust for TPN (Lehtinen et al. 1998) and the WTAK clouds (Ward-Thompson et al. 2002). The only cloud containing a young stellar object, DC 303.8–14.2, seems to be no different to the other clouds if we exclude the emission from the IRAS source within DC 303. Based on the parameters given in Table 3, we cannot distinguish the star forming cloud from non-star forming ones based on diffuse far-IR emission of dust.

6. Conclusions

We have observed with the ISOPHOT instrument at far-IR wavelengths the globule DC 303.8–14.2 and the embedded young stellar object IRAS 13036–7644. The dust temperature and circumstellar mass of the IRAS source are about 20 K and 0.1 $M_\odot$, respectively. The bolometric luminosity is ∼1.0 $L_\odot$. We classify the source as a transition object between Class 0 and I in a late accretion phase. The IRAS source was detected at 7.7 μm with a flux of about 0.16 Jy. This emission is suggested to be mostly *UIR* band emission.

The properties of dust in DC 303.8–14.2 have been compared with those in the Thumbprint Nebula, a morphologically similar cloud but without signs of star formation. We find no difference in the density distributions between these two clouds. The dust temperature is about 1 K higher and the dust column density is about 1.7 times higher in DC 303.8–14.2 than in the TPN.

Extended 7.7 μm emission has been detected from the outer parts of DC 303.8–14.2 and there is tentative evidence that the maximum of the 7.7 μm emission is located at the edge of the optical extent of the globule. This is most probably due to a halo-like distribution of very small dust particles or PAHs emitting at 7.7 μm.

Comparison of DC 303.8–14.2 with several clouds without YSOs shows that a cloud with low-mass star formation cannot be distinquished from non-star forming clouds on the basis of the properties of far-IR diffuse emission of 'classical large' dust particles.

Acknowledgements. The work of K.L. and K.M. has been supported by the Research Council for Natural Sciences and Engineering through grant Nos. 17854 and 176071, which are gratefully acknowledged. We thank Carlos Gabriel for providing the IDL runtime version of PIA. ISOPHOT and the Data Centre at MPIA, Heidelberg, are funded by the Deutsches Zentrum für Luft- und Raumfahrt DLR and the Max-Planck-Gesellschaft.

The UK Schmidt Telescope was operated by the Royal Observatory Edinburgh, with funding from the UK Science and Engineering Research Council (later the UK Particle Physics and Astronomy Research Council), until 1988 June, and thereafter by the Anglo-Australian Observatory. The blue plates of the southern Sky Atlas and its Equatorial Extension (together known as the SERC-J), as well as the Equatorial Red (ER) and the Second Epoch [red] Survey (SES) were all taken with the UK Schmidt.

The Digitized Sky Survey was produced at the Space Telescope Science Institute under US Government grant NAG W-2166. The images of these surveys are based on photographic data obtained using the Oschin Schmidt Telescope on Palomar Mountain and the UK Schmidt Telescope. The plates were processed into the present compressed digital form with the permission of these institutions.

References

Adams, F. C., Lada, C. J., & Shu, F. H. 1987, ApJ, 312, 788
Adams, F. C. 1991, ApJ, 382, 544
André, P., Ward-Thompson, D., Barsony, & M. 1993, ApJ, 406, 122
André, P., & Montmerle, T. 1994, ApJ, 420, 837
Bernard, J. P., Boulanger, F., Desert, F. X., & Puget, J. L. 1992, A&A, 263, 258
Bernard, J. P., Boulanger, F., & Puget, J. L. 1993, A&A, 277, 609
Bourke, T. L., Hyland, A. R., & Robinson, G. 1995, MNRAS, 276, 1052
Casali, M. M. 1986, MNRAS, 223, 341
Chen, H., Myers, P. C., Ladd, E. F., et al. 1995, ApJ, 445, 377
Chen, H., Grenfell, T. G., Myers, P. C., & Hughes, J. D. 1997, ApJ, 478, 295
Chini, R., Krügel, E., & Wargau, W. 1987, A&A, 181, 378
Chini, R., Ward-Thompson, D., Kirk, J. M., et al. 2001, A&A, 369, 155
Clemens, D. P., & Barvainis, R. 1988 ApJS, 68, 257
Clemens, D. P., João, L. Y., & Heyer, M. H. 1991, ApJS, 75, 877
Crutcher, R. M., Nutter, D. J., Ward-Thompson, D., & Kirk, J. M. 2004, ApJ, 600, 279
Dent, W. R. F., Furuya, R. S., & Davis, C. J. 2003, MNRAS, 339, 633
Feitzinger, J. A., & Stuve, J. V. 1984, A&AS, 58, 365
Gabriel, C., Acosta-Pulido, J., Heinrichsen, I., Morris, H., & Tai, W.-M. 1997, The ISOPHOT Interactive Analysis PIA, a calibration and scientific analysis tool, in Astronomical Data Analysis Software and Systems (ADASS) VI, ed. G. Hunt, & H. E. Payne (San Francisco: ASP), ASP Conf. Ser., 125, 108
Garay, G., Mardones, D., & Rodríguez, L. F., et al. 2002, ApJ, 567, 980
Gauvin, L. S., & Strom, K. M. 1992, ApJ, 385, 217
Good, J. C. 1994, Zodiacal dust cloud modeling using IRAS data; IRAS Sky Survey Atlas: Explanatory Supplement; S. L. Wheelock, T. N. Gautier, J. Chillemi, D. Kester, H. McCallon, C. Oken, J. White, D. Gregorich, F. Boulanger, and J. Good; G1-G14; JPL Publication 94, Pasadena
Hartley, M., Manchester, R. N., Smith, R. M., Tritton, S. B., & Goss, W. M. 1986, A&AS, 63, 27
Henning, Th., Pfau, W., Zinnecker, H., & Prusti, T. 1993, A&A, 276, 129
Hughes, J., & Hartigan, P. 1992, AJ, 104, 680
Jones, B. F., & Herbig, G. H. 1979, AJ, 84, 1872
Juvela, M., Mattila, K., Lehtinen, K., et al. 2002, A&A, 382, 583
Kainulainen, J. 2004, Master's Thesis, University of Helsinki
Kenyon, S. J., Calvet, N., & Hartmann, L. 1993, ApJ, 414, 676
Kenyon, S. J., Whitney, B. A., Gomez, M., & Hartmann, L. 1993, ApJ, 414, 773
Kessler, M. F., Steinz, J. A., Anderegg, M. E., et al. 1996, A&A, 315, L27
Knude, J., & Høg, E. 1998, A&A, 338, 897
Kukarkin, B. V., et al. 1971, General Catalogue of Variable Stars, 3rd ed.
Lada, C. J., & Wilking, B. 1984, ApJ, 287, 610
Lada, C. J. 1987, in Star Forming Regions, ed. Peimbert M., Jugaku J. (Dordrecht: Reidel), IAU Symp. No., 115, 1
Laureijs, R. J. Haikala, L. Burgdorf, M., et al. 1996, A&A, 315, L317
Lee, M. H., & Rogers, C. 1987, ApJ, 317, 197
Lehtinen, K., & Mattila, K. 1996, A&A, 309, 570
Lehtinen, K. 1997, A&A, 317, L5
Lehtinen, K., Lemke, D., Mattila, K., & Haikala, L. K. 1998, A&A, 333, 702
Lehtinen, K., Mattila, K., & Lemke, D. 2000, ISO Beyond Point Sources: Studies of Extended Infrared Emission, Madrid, Spain, April 2000, ESA SP-455
Lehtinen, K., Mattila, K., Russeil, D., et al. 2001, Proc. of the Conference The Calibration Legacy of the ISO Mission, VILSPA, Spain, February 2001, ESA SP-481
Lehtinen, K., & Higdon, J. L. 2003a, A&A, 398, 583
Lehtinen, K., Mattila, K., Lemke, D., et al. 2003b, A&A, 398, 571
Lehtinen, K., Mattila, K., Väisänen, P., & Knude, J., ESO Press Photo 26a/03, http://www.eso.org/outreach/press-rel/pr-2003/phot-26-03.html
Lemke, D., Klaas, U., Abolins, J., et al. 1996, A&A, 315, L64
Leung, C. M., O'Brien, E. V., & Dubisch, R. 1989, ApJ, 337, 293
Lucas, P. W., & Roche, P. F. 1997, MNRAS, 286, 895
Morris, P. W., Noriega-Crespo, A., Marleau, F. R., et al. 2004, ApJS, 154, 339
Myers, P. C., & Ladd, E. F. 1993, ApJ, 413, L47
Ossenkopf, V., & Henning, Th. 1994, A&A, 291, 943
Persi, P., & Tapia, M. 2003, A&A, 406, 149
Pezzuto, S., Grillo, F., Benedettini, M., et al. 2002, MNRAS, 330, 1034
Prusti, T., Whittet, D. C. B., Assendorp, R., & Wesselius, P. R. 1992, A&A, 260, 151
Rawlings, M. G., Juvela, M., Mattila, K., et al. 2004, in press
Richards, P. J., Knee, L. B. G., Russell, S. C., & Haas, M. 1999, in The Universe As Seen By ISO, ed. Cox P., & Kessler, M. F., ESA SP–427, 513
Santos, N. C., Yun, J. L., Santos, C. A., & Marreiros, R. G. 1998, ApJ, 116, 1376
Schutte, W. A., Tielens, A. G. G. M., Allamandola, L. J., et al. 1990, ApJ, 360, 577
Spencer, R. G., & Leung, C. M. 1978, ApJ, 222, 140
Tafalla, M., Myers, P. C., Mardones, D., et al. 2000, A&A, 359, 967
Tóth, L. V., Kiss, Cs., Juvela, M., et al. 2002, A&A, 395, 663
Visser, A. E., Richer, J. S., & Chandler, C. J. 2002, AJ, 124, 2756
Whitney, B. A., & Hartmann, L. 1993, ApJ, 402, 605
Wilking, B. A., Lada, C. J., & Young, E. T. 1989, ApJ, 340, 823
Ward-Thompson, D., Scott, P. F., Hills, R. E., & André, P. 1994, MNRAS, 268, 276
Ward-Thompson, D., Motte, F., & André, P. 1999, MNRAS, 305, 143
Ward-Thompson, D., André, P., & Kirk, J. M. 2002, MNRAS, 329, 257
Yun, J. L., & Clemens, D. P. 1991, ApJ, 381, 474